3D angle decomposition for elastic reverse time migration

Yuting Duan & Paul Sava, Center for Wave Phenomena, Colorado School of Mines*

SUMMARY

We propose 3D angle decomposition methods from elastic reverse time migration using time- and space-lag common image point gathers, time-lag common image gathers, and space-lag common image gathers computed by elastic wavefield migration. We compute time-lag common image gathers at multiple contiguous locations, instead of isolated positions as is commonly done with common image gathers. Then, we transform the extended images to the angle domain using slant stacks along surfaces that connect neighboring positions, instead of line slant stacks for isolated common image gathers. We demonstrate our methods using 2D and 3D synthetic examples and show that our techniques provide accurate opening and azimuth angles, and that they can handle steeply dipping reflectors and converted wave modes.

INTRODUCTION

Common reflection-angle gathers are useful in migration velocity analysis and amplitude-versus-angle analysis. Among angle decomposition techniques, wavefield-based methods are preferred because they accurately simulate wave propagation in complex geologic structures. Wavefield-based methods generally fall into two categories: pre-migration and post-migration algorithms (Vyas et al., 2011). Pre-migration methods decompose the wavefields prior to the imaging condition, for example by $f-k$ domain decomposition, (Xu et al., 2011), or by Poynting vector methods (Yoon and Marfurt, 2006; Yan et al., 2013). Post-migration methods, transform extended images to angle gathers after the imaging condition, using space-lag or time-lag common image gathers (CIG), and mixed time- and space-lags common image point (CIP) gathers (De Bruin et al., 1990; Sava and Fomel, 2003; Biondi and Symes, 2004; Sava and Vlad, 2011). Compared to pre-migration algorithms, post-migration methods are cheaper and can handle complicated wavefields.

Angle decomposition methods can also be applied to elastic wavefields. In contrast to acoustic wavefields, elastic wavefields contain various wave modes (e.g. P and S waves). Yan and Xie (2012) suggest a pre-migration method for angle decomposition in elastic media, while Yan and Sava (2008) propose post-migration decomposition methods involving wave mode decomposition. Duan and Sava (2015) further develop a scalar imaging condition for converted waves, which generates 3D PS and SP scalar images cheaply and without explicit polarity correction.

In this paper, we present methods for opening and azimuth angle decomposition from elastic RTM images. We develop the extended scalar imaging condition which generalizes the zero-lag scalar imaging condition (Duan and Sava, 2015). Our methods utilize local plane wave decompositions of extended images and exploit the relationships between the time-lag, space-lag, and image shift in space, which are measured in extended images. These relationships lead to opening and azimuth angle decomposition methods using either time-lag common image gather (τCIGs), space-lag common image gathers (λCIGs), or time- and space-lag common image point (CIP) gathers. We demonstrate the algorithms with 3D elastic time- and space-lag CIPs and 2D elastic time-lag extended images evaluated at multiple contiguous positions.

ELASTIC SCALAR IMAGING CONDITION

Duan and Sava (2015) propose a scalar imaging condition using geometrical relationships between the propagation directions for the P and S waves and the reflector orientation. The PS and SP images computed using this imaging condition are scalars without polarity reversals. Here, we develop a more general form of extended imaging conditions as a function of space and crosscorrelation lags (space-lag λ and time-lag τ):

$$I^{PP}(\mathbf{x},\lambda,\tau) = \sum_{e,t} P_s(e,\mathbf{x}-\lambda,t-\tau)\, P_r(e,\mathbf{x}+\lambda,t+\tau)\ , \qquad (1)$$

$$I^{PS}(\mathbf{x},\lambda,\tau) = \sum_{e,t} [\nabla P_s(e,\mathbf{x}-\lambda,t-\tau)\times \mathbf{n}(\mathbf{x})]\cdot \mathbf{S}_r(e,\mathbf{x}+\lambda,t+\tau)\ , \qquad (2)$$

$$I^{SP}(\mathbf{x},\lambda,\tau) = \sum_{e,t} [\nabla\times \mathbf{S}_s(e,\mathbf{x}-\lambda,t-\tau)\cdot \mathbf{n}(\mathbf{x})]\, P_r(e,\mathbf{x}+\lambda,t+\tau)\ , \qquad (3)$$

$$I^{SS}(\mathbf{x},\lambda,\tau) = \sum_{e,t} \mathbf{S}_s(e,\mathbf{x}-\lambda,t-\tau)\cdot \mathbf{S}_r(e,\mathbf{x}+\lambda,t+\tau)\ . \qquad (4)$$

Vector $\mathbf{n}(\mathbf{x})$ is the normal to the reflector plane. Quantities $\mathbf{S}(e,\mathbf{x},t)$ and $P(e,\mathbf{x},t)$ represent P and S wavefields obtained by wave-mode decomposition, as functions of experiment e, time t, and space $\mathbf{x}$. Subscripts s and r indicate the wavefield origins at source or receivers, respectively. P and S wavefields are obtained from displacement field using Helmholtz decomposition (Dellinger and Etgen, 1990; Yan and Sava, 2008):

$$P(e,\mathbf{x},t) = \nabla\cdot\mathbf{u}(e,\mathbf{x},t)\ , \qquad (5)$$

$$\mathbf{S}(e,\mathbf{x},t) = \nabla\times\mathbf{u}(e,\mathbf{x},t)\ . \qquad (6)$$

MOVEOUT ANALYSIS

The extended imaging condition in equations 1-4 preserves necessary information for decomposing images in angle-dependent components, which can be used for velocity analysis. In 3D, the PP, PS, SP, and SS images generated using this imaging condition are scalars, which can be used directly to construct angle gathers. We formulate our method under the assumption that the reflector is locally planar, and that the incident and

reflected wavefields are also locally planar. However, the derived algorithms are not limited to cases where the wavefronts are planar, because waves can always be decomposed to planar components, even in complex wavefields characterized by multipathing.

We define the angle domain as the set of half-opening angle θ, and azimuth ϕ, $\{\theta,\phi\}$. The (planar) source wavefield propagates along the direction indicated by vector $\mathbf{n}_s$ with speed v_s, and the (planar) receiver wavefield propagates along the direction indicated by vector $\mathbf{n}_r$ with speed v_r. Quantity $\mathbf{x}_o$ indicates the intersection of the two wavefronts at time $t = t_o$:

$$\begin{cases} \mathbf{n}_s \cdot (\mathbf{x}-\mathbf{x}_o) = v_s\,(t-t_o)\ , & (7) \\ \mathbf{n}_r \cdot (\mathbf{x}-\mathbf{x}_o) = v_r\,(t-t_o)\ . & (8) \end{cases}$$

The time-lag τ and space-lags λ in equations 7 and 7 represent movement of the wavefronts in time and space, respectively. Then, the intersection of the two wavefronts shifts to a new position $\mathbf{x}$. The geometrical expressions for the extended imaging condition using the planar source and receiver wavefields are

$$\begin{cases} \left(\dfrac{\mathbf{n}_s}{v_s}-\dfrac{\mathbf{n}_r}{v_r}\right)\cdot(\mathbf{x}-\mathbf{x}_o)-\left(\dfrac{\mathbf{n}_s}{v_s}+\dfrac{\mathbf{n}_r}{v_r}\right)\cdot\lambda = -2\tau\ , & (9) \\ \left(\dfrac{\mathbf{n}_s}{v_s}+\dfrac{\mathbf{n}_r}{v_r}\right)\cdot(\mathbf{x}-\mathbf{x}_o)-\left(\dfrac{\mathbf{n}_s}{v_s}-\dfrac{\mathbf{n}_r}{v_r}\right)\cdot\lambda = 0\ , & (10) \end{cases}$$

where vector $(\mathbf{x}-\mathbf{x}_o)$ measures the spatial shift of the image point, corresponding to time-lag τ and space-lag λ.

We consider three types of extended images, using both space- and time-lags, or using time-lag, or using space-lags. In the following, we derive the equations that link the space and/or time lags with half-opening θ and azimuth ϕ angles from equations 9 and 10.

Angle decomposition using CIPs

For CIP gathers, we set the image shift $\mathbf{x}-\mathbf{x}_o = \mathbf{0}$ in equations 9 and 10, and replace vectors $\mathbf{n}_s$ and $\mathbf{n}_r$ with vectors $\mathbf{q}$, $\mathbf{n}$ and angle θ. Quantity $\mathbf{n}$ is the local normal vector, and $\mathbf{q}$ is the vector lying at the intersection of the interface and the reflection plane, thus it is a function of the azimuth angle ϕ. We obtain the system of equations that describes the relationships between image shift $(\mathbf{x}-\mathbf{x}_o)$ and time-lag τ:

$$\begin{cases} \dfrac{\gamma\sin 2\theta}{\sqrt{\gamma^2+1+2\gamma\cos 2\theta}}\,(\mathbf{q}\cdot\lambda) = v_s\tau\ , & (11) \\ \mathbf{n}\cdot\lambda = 0\ . & (12) \end{cases}$$

where quantity γ is the ratio of v_s and v_r. For angle decomposition, we loop over all possible values of the reflection angles, θ and ϕ, and slant-stack the extended image $\mathbf{I}(\lambda,\tau)$ using equations 11 and 12 to produce the angle-domain image $\mathbf{I}(\phi,\theta)$. Equations 11 and 12 simplify to the acoustic case, with velocity ratio $\gamma = 1$ Sava and Vlad (2011):

$$\begin{cases} \sin\theta\,(\mathbf{q}\cdot\lambda) = v_s\tau\ , & (13) \\ \mathbf{n}\cdot\lambda = 0\ . & (14) \end{cases}$$

We illustrate our angle decomposition methodology using a simple example of a 3D homogeneous model with a horizontal reflector at depth $z = 0.2$ km. The acquisition geometry consists of a vertical displacement source at $\{0.4, 0.4, 0.02\}$ km and a 2D network of receivers at $z = 0.02$ km. We compute the PS image (Figure 1a) and an angle gather (Figure 1b) at coordinates $\{0.2, 0.2, 0.2\}$ km. The dot overlain on the angle gather image is the analytical solution of the opening and azimuth angles for this specific acquisition geometry.

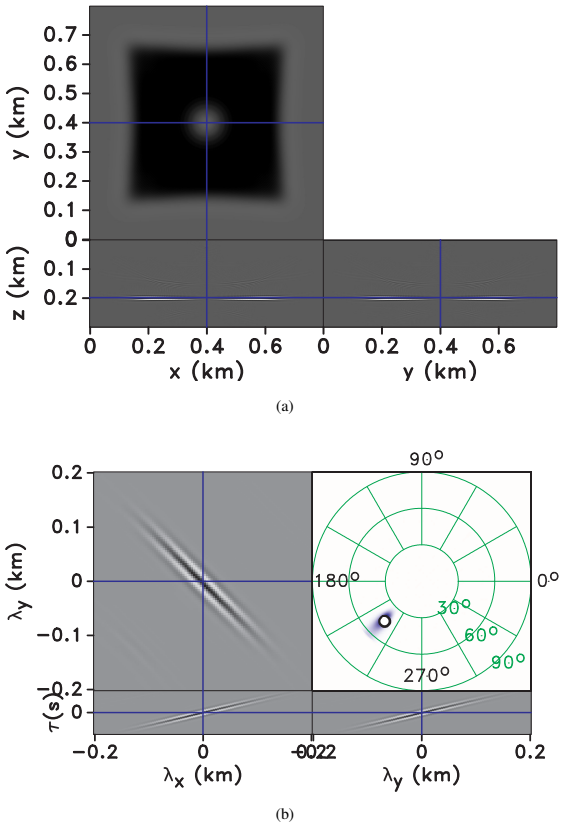

Figure 1: (a) PS image computed for one shot. (b)Extended CIP and 3D angle gather for the PS image at coordinates $\{0.2, 0.2, 0.2\}$ km. The dot represents the analytical estimation of the opening and azimuth angle using the acquisition geometry.

Angle decomposition using time-lag CIGs

For τCIGs, we set the space-lag $\lambda = \mathbf{0}$ in equations 9 and 10, and replace vector $\mathbf{n}_s$ and $\mathbf{n}_r$ with vector $\mathbf{q}$, $\mathbf{n}$ and angle θ. The system of equations that describes the relationships between image shift $(\mathbf{x}-\mathbf{x}_o)$ and time-lag τ is:

$$\begin{cases} \dfrac{\sqrt{\gamma^2+1+2\gamma\cos 2\theta}}{2}\,[\mathbf{n}\cdot(\mathbf{x}-\mathbf{x}_o)] = v_s\tau\ , & (15) \\ \sin 2\theta\sqrt{\gamma^2+1+2\gamma\cos 2\theta}\,[\mathbf{q}\cdot(\mathbf{x}-\mathbf{x}_o)] = v_s\tau\dfrac{1-\gamma^2}{\gamma}\ , & (16) \end{cases}$$

where equation 15 corresponds to the projection of the image shift $(\mathbf{x}-\mathbf{x}_o)$ on the reflector normal $\mathbf{n}$, and equation 16 corresponds to the projection of the image shift $(\mathbf{x}-\mathbf{x}_o)$ on vector $\mathbf{q}$. For angle decomposition, we loop over all possible values of the reflection angles, θ and ϕ, and slant stack the extended image $\mathbf{I}(\mathbf{x},\tau)$ using equations 15 and 16 to produce the angle-domain image $\mathbf{I}(\phi,\theta)$. Equations 15 and 16 simplify to

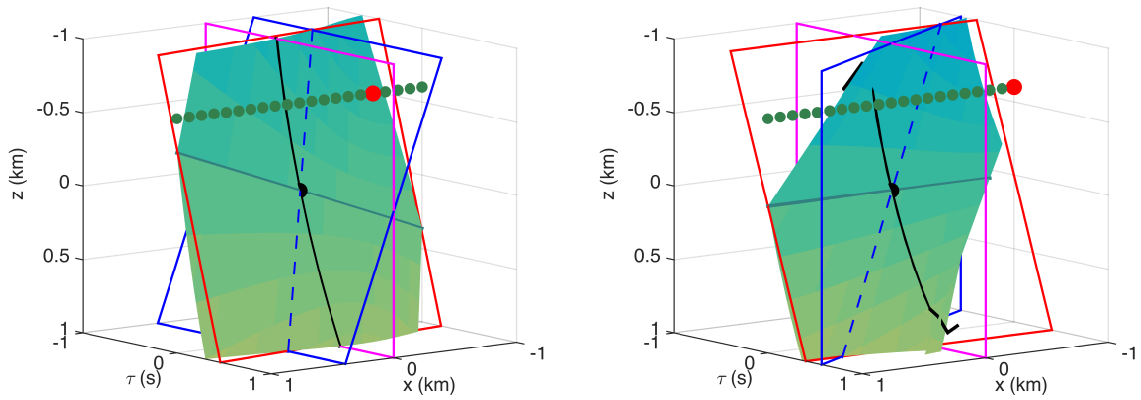

Figure 2: Predicted spatial shift for (a) dipping and (b) horizontal reflectors imaged using PP and PS data, respectively. The large red dots represents the source locations, and the line of smaller green dots represents receiver positions.

the acoustic case, with velocity ratio $\gamma = 1$ (Sava and Fomel, 2006):

$$\begin{cases} \cos\theta\,[\mathbf{n}\cdot(\mathbf{x}-\mathbf{x}_o)] = v_s\tau\,, & (17) \\ \mathbf{q}\cdot(\mathbf{x}-\mathbf{x}_o) = 0\,. & (18) \end{cases}$$

Note that in equations 17 and 18, time-lag τ is not related to vector $\mathbf{q}$, i.e., the time-lag extended images do not contain azimuthal information for the acoustic case. However, for converted waves ($\gamma \neq 1$), time-lag extended images contain azimuthal information according to equations 15 and 16.

We illustrate the time-lag algorithm with 2D examples. Consider a model with a dipping reflector in the P-velocity. Using equations 17 and 18, we can predict the spatial shift of the reflector as a function of time-lag τ, Figure 2a. The dashed line is the intersection of two planes (equations 17 and 18), which illustrates the spatial shift for image point at $x = 0.0$ km, $z = 0.0$ km. The solid line through the image point represents the analytical moveout of the extended image in a vertical CIG. The dashed and solid lines do not coincide with one-another, i.e., the method that applies a slant stack to a vertical CIG at a single x location does not measure the image shift $(\mathbf{x}-\mathbf{x}_o)$ accurately. The angle gathers computed using this method and the method using a slant stack along the surface are shown in the middle and right panels of Figure 3a, respectively. The surface slant stack leads to more focused angle gathers, indicating significantly higher accuracy.

Similarly, for converted waves, the image does not only shift vertically, but also horizontally in the time-lag gather even for a horizontal reflector. The predicted spatial shift of the reflector is shown in Figure 2b. The first panel in Figure 3b shows the computed extended image gather at $x = 0.0$ km. Note that the shape of the extended image in this panel is curved. The angle gathers computed using a line slant stack for this gather and a surface slant stack are shown in the middle and right panels of Figure 3b, respectively. As for the preceding example, we obtain more focused angle gathers using the surface slant stack.

ANGLE DECOMPOSITION USING SPACE-LAG CIG

For λCIGs, we set $\tau = 0$ in equations 9 and 10, and replace vector $\mathbf{n}_s$ and $\mathbf{n}_r$ with vector $\mathbf{q}$, $\mathbf{n}$ and angle θ. The system of equations that describes the relationships between image shift $(\mathbf{x}-\mathbf{x}_o)$ and space-lag λ is:

$$\begin{cases} \dfrac{\gamma^2+1+2\gamma\cos 2\theta}{2\gamma}\mathbf{n}\cdot(\mathbf{x}-\mathbf{x}_o)+\sin 2\theta\,\mathbf{q}\cdot\lambda = \dfrac{1-\gamma^2}{2\gamma}\mathbf{n}\cdot\lambda\,, & (19) \\ \dfrac{\gamma^2+1+2\gamma\cos 2\theta}{2\gamma}\mathbf{n}\cdot\lambda+\sin 2\theta\,\mathbf{q}\cdot(\mathbf{x}-\mathbf{x}_o) = \dfrac{1-\gamma^2}{2\gamma}\mathbf{n}\cdot(\mathbf{x}-\mathbf{x}_o) & (20) \end{cases}$$

For angle decomposition, we loop over all possible values of the reflection angles, θ and ϕ, and slant stack the extended image $\mathbf{I}(\mathbf{x},\lambda)$ using equations 19 and 20 to produce the angle-domain image $\mathbf{I}(\phi,\theta)$.

EXAMPLES

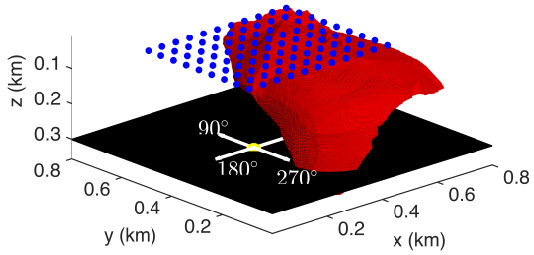

Figure 4: 3D salt body based on the SEG/EAGE model, showing the position of the image point at $\{0.3, 0.4, 0.3\}$ km, and the sources on the surface.

For simple geologic models, subsurface illumination from different opening and azimuth angles tends to be uniform. However, in areas with complex geologic structures, such as salt

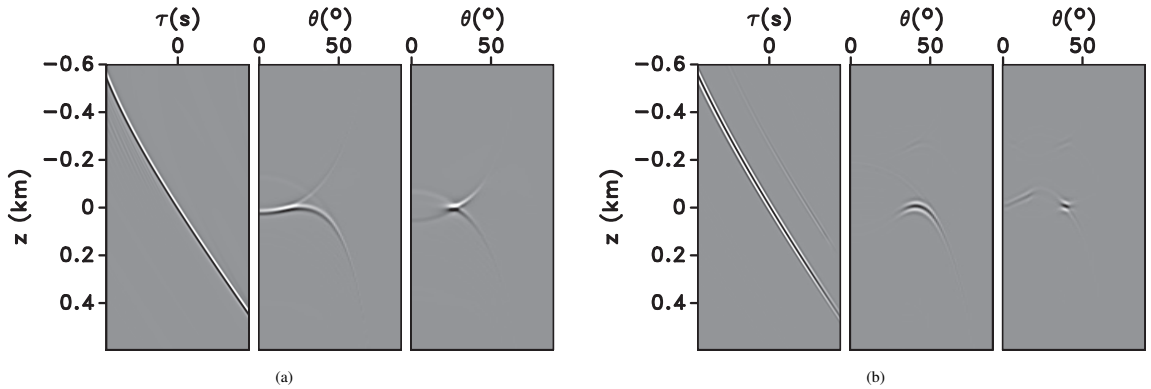

Figure 3: Extended image gathers for (a) PP and (b) PS reflections. From left to right, the panels depict the extended image, and the angle gathers constructed using line or surface slant stacks, respectively.

bodies, severe wavefield distortions lead to irregular subsurface illumination, even if acquisition is uniform. Angle gathers characterize subsalt illumination, which benefits reservoir characterization and acquisition design.

We show an angle gather computed using the proposed elastic angle decomposition methodologies for a modified version of the SEG/EAGE salt model (Aminzadeh et al., 1996). We add a horizontal reflector at $z = 0.3$ km, and compute the opening and azimuth angles for an image point on the horizontal reflector at coordinates $x = 0.3$ km, $y = 0.4$ km. The acquisition geometry contains 91 sources and a 2D network of receivers at $z = 0.02$ km. We generate three-component shot gathers using a vertical displacement source with a 100 Hz peak frequency Ricker wavelet. As shown in Figure 4, due to the existence of the salt body, it is difficult to illuminate the considered image point from certain azimuths, as seen in Figures 5a-5b. Both angle gathers show similar illumination patterns. The PP image is mainly illuminated from north-west and south-east, and the PS image is illuminated from west and south-east (0° indicates due East). Compared to the PP angle gather, the PS angle gather has higher resolution, since the S wavelength is generally smaller than the P wavelength.

CONCLUSIONS

Elastic 3D angle decomposition can be performed on time-lag or space-lag common image gathers, as well as on mixed time-/space-lag common image point gathers. We propose extended imaging conditions to compute scalar PP, PS, SP, and SS images, and algorithms for computing opening and azimuth angle gathers. Our algorithms generate accurate angle gathers if we consider the complete slant-stack surface, instead of the more popular slant stacks along lines defined in common image gathers at fixed surface positions. Our 2D and 3D examples show that the algorithms can handle dipping reflectors and images generated using converted waves.

ACKNOWLEDGMENTS

We thank the sponsors of the Center for Wave Phenomena, whose support made this research possible. The reproducible numeric examples in this paper use the Madagascar open-source software package (Fomel et al., 2013) freely available from http://www.ahay.org. The authors thank Paul Fowler for helpful discussions and valuable suggestions.

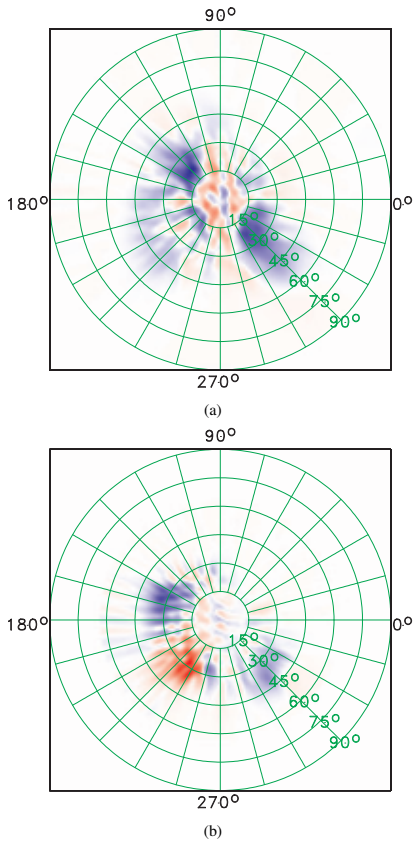

Figure 5: Opening and azimuth angle gather computed using (a) PP and (b) PS elastic reflections.

REFERENCES

Aminzadeh, F., N. Burkhard, J. Long, T. Kunz, and P. Duclos, 1996, Three dimensional SEG/EAEG models-an update: The Leading Edge, **15**, 131–134.

Biondi, B., and W. W. Symes, 2004, Angle-domain common-image gathers for migration velocity analysis by wavefield-continuation imaging: Geophysics, **69**, 1283–1298.

De Bruin, C., C. Wapenaar, and A. Berkhout, 1990, Angle-dependent reflectivity by means of prestack migration: Geophysics, **55**, 1223–1234.

Dellinger, J., and J. Etgen, 1990, Wave-field separation in two-dimensional anisotropic media: Geophysics, **55**, 914–919.

Duan, Y., and P. Sava, 2015, Scalar imaging condition for elastic reverse time migration: Geophysics, **80**, S127–S136.

Fomel, S., P. Sava, I. Vlad, Y. Liu, and V. Bashkardin, 2013, Madagascar: open-source software project for multidimensional data analysis and reproducible computational experiments: Journal of Open Research Software, **1**, e8.

Sava, P., and S. Fomel, 2006, Time-shift imaging condition in seismic migration: Geophysics, **71**, S209–S217.

Sava, P. C., and S. Fomel, 2003, Angle-domain common-image gathers by wavefield continuation methods: Geophysics, **68(3)**, 1065–1074.

Sava, P. C., and I. Vlad, 2011, Wide-azimuth angle gathers for wave-equation migration: Geophysics, **76(3)**, S131–S141.

Vyas, M., X. Du, E. Mobley, and R. Fletcher, 2011, Methods for computing angle gathers using RTM: Presented at the 73rd EAGE Conference & Exhibition.

Xu, S., Y. Zhang, and B. Tang, 2011, 3D angle gathers from reverse time migration: Geophysics, **76(2)**, S77–S92.

Yan, J., W. Ross, et al., 2013, Improving the stability of angle gather computation using Poynting vectors: Presented at the 2013 SEG Annual Meeting, Society of Exploration Geophysicists.

Yan, J., and P. Sava, 2008, Isotropic angle-domain elastic reverse-time migration: Geophysics, **73(6)**, S229–S239.

Yan, R., and X.-B. Xie, 2012, An angle-domain imaging condition for elastic reverse time migration and its application to angle gather extraction: Geophysics, **77(5)**, S105–S115.

Yoon, K., and K. J. Marfurt, 2006, Reverse-time migration using the Poynting vector: Exploration Geophysics, **37**, 102–107.